

Magnetic penetration depth of superconducting Aluminum thin films

David López-Núñez,^{1,2,3} Queralt Portell-Montserrat,^{1,4,5} Gemma Rius,⁴
Elia Bertoldo,¹ Alba Torras-Coloma,^{1,5} M. Martínez,^{1,6} and P. Forn-Díaz^{1,6,*}

¹*Institut de Física d'Altes Energies, The Barcelona Institute of Science and Technology, Bellaterra 08193, Spain*

²*Departament de Física Quàntica i Astrofísica and Institut de*

Ciències del Cosmos, Universitat de Barcelona, Barcelona 08028, Spain

³*Barcelona Supercomputing Center, Barcelona 08034, Spain*

⁴*Institute of Microelectronics of Barcelona (IMB-CNM), Spanish National Research Council (CSIC), Cerdanyola 08193, Spain*

⁵*Departament de Física, Universitat Autònoma de Barcelona, 08193 Bellaterra, Spain*

⁶*Qilimanjaro Quantum Tech SL, Barcelona, Spain*

We present a study of the magnetic penetration depth λ in superconducting aluminum thin films of varying thickness. The range of thicknesses chosen spans from the thin-film regime to the regime approaching bulk behaviour. The penetration depth values estimated range from $\lambda = 163.3 \pm 0.4$ nm for the thinnest 20 nm samples down to $\lambda = 53.6 \pm 0.4$ nm for the 200 nm-thick ones. In order to accurately determine λ , we performed complementary measurements using the resonance frequency of superconducting LC resonators and the normal-state resistance of meander structures. Both methods yield comparable results, providing a well-characterized set of values of λ in aluminum in the relevant range for applications in fields such as quantum computing and microwave radiation detector technologies.

I. INTRODUCTION

Bulk aluminum has been an extensively studied material in the literature [1], widely considered as the archetype material of type-I conventional superconductivity. In contrast, the properties of thin-film aluminum, conventionally utilized in, e.g., quantum computing technologies [2–5] and kinetic inductance detectors [6], have received limited attention. Specifically, thin-film aluminum exhibits type-II superconductivity [7], resulting in a complete distinct behavior than its bulk version.

In type-II superconductors, the short range of Cooper pairs results in the emergence of normal-metal paths, leading to the appearance of vortices within the material [8]. Furthermore, type-II superconductors may exhibit a significantly large kinetic inductance, L_k , comparable or larger than their geometric inductance, L_g [9, 10]. Accurately determining L_k is important as it needs to be taken into account, e.g., in the design of quantum circuits [10, 11], requiring a thorough material characterization, particularly concerning the magnetic penetration depth, λ . The parameter λ is intrinsically material-dependent and represents the distance a magnetic field parallel to the surface penetrates into a superconductor. External factors such as the presence of impurities, the thickness of the film, or the direction of the magnetic field lead to an effective value of λ [12]. In particular, the film thickness strongly influences microscopic properties such as the electrical resistivity and the electron mean-free path [13–15], which then modify the value of λ . To the best of our knowledge, the relationship between thickness and penetration depth in aluminum has not been extensively investigated nor documented in the existing literature.

In this work, we determine λ of thin-film aluminum for samples with various film thicknesses by two complementary methods. In a first method we measured the resonance frequency of a number of lumped-element superconducting resonators, while in a second method we evaluated the low-temperature resistance of thin-film test structures. These methodologies align with previous investigations conducted on other superconducting materials, such as Nb [16], NbN [17] and granular aluminum [18]. In addition to λ , both methods combined allow us to characterize L_k for all thicknesses studied. In order to properly evaluate λ , we have developed a new fitting method for resonator devices with accurate error estimation. Finally, our investigation yields an estimate of the range of film thicknesses at which the transition occurs between the type-II superconductivity exhibited by thin-film aluminum and the type-I superconductivity characteristic of vortex-free, bulk aluminum. This transition may be relevant for superconducting qubits [19, 20] and resonators [7] since the presence of vortices may degrade the quality of devices made of thin-film aluminum. In summary, the methods and results obtained in this work represent an important resource in the design of thin-film aluminum-based quantum circuits.

The outline of this work is as follows: Section II introduces the theoretical aspects of superconductivity needed for the data analysis. In section III, the methods used in this work to extract the penetration depth λ are described. Section VI presents the simulation methods along with the device characteristics. Section V focuses on the experimental methodology. The experimental results are discussed in Sec. VI. Finally, Sec. VII presents the conclusions of this work.

* pfordiaz@ifae.es

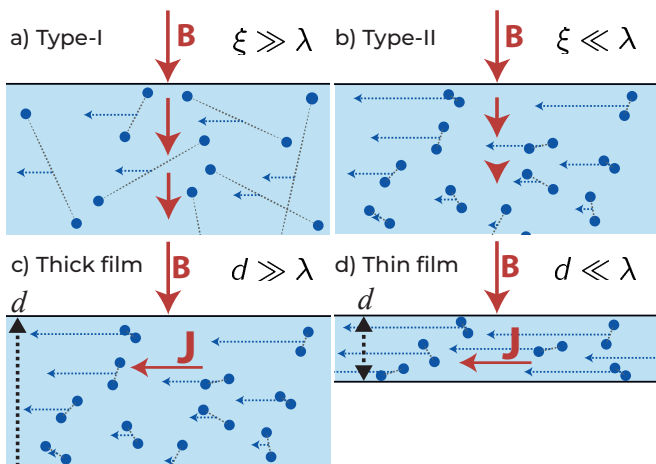


FIG. 1. **a)** Type-I superconductors, where response to an external perpendicular magnetic field is non-local. Each Cooper pair reacts to the magnetic field at its center of mass, since the average Cooper pair size ξ is much larger than the typical distance at which the magnetic field decays, λ . This effectively reduces the field response, allowing the magnetic field to penetrate further into the material, thus increasing the penetration depth. **b)** In type-II superconductors, ξ is smaller than λ , and the response is local, since both electrons of the Cooper pair are very close. **c)** Schematic representation of a local thick superconductor of thickness d with $d \gg \lambda$, where the London equations are valid. The current response to the magnetic field follows $\vec{j}_S = -\frac{\mu_0}{\lambda^2} \vec{A}_S$. The length of arrows represents the velocity of Copper pairs. **d)** In very thin films where $d \lesssim \lambda$, the Cooper pair number density is lower, all Cooper pairs have to increase their velocity compared to thicker films to provide the same supercurrent \vec{j}_S , since the London equations are still valid. The kinetic inductance increases dramatically in this situation, as it is proportional to the squared velocity, $L_k \propto v^2$.

II. THEORETICAL BACKGROUND

In general, the superconductivity type exhibited by a given material reflects the interplay between the magnetic penetration depth λ and its coherence length ξ , which corresponds to the average distance between the electrons forming a Cooper pair [21].

The thickness of a thin film affects its internal microscopic structure, modifying both λ and ξ and the rest of parameters that depend on them. In particular, the kinetic inductance L_k has a strong dependence on λ through [18, 22–24]

$$L_k = L_{k,s} N = \mu_0 \lambda N, \quad (1)$$

where $L_{k,s}$ is the surface kinetic inductance, or kinetic inductance per square, which depends on the film thickness d . N is the number of squares of a given wire. For wires with constant cross section, we have $N = l/w$, where l and w are the wire length and width, respectively. Otherwise, N becomes a position-dependent parameter.

In bulk aluminum, the response of the superconductor to magnetic fields is non-local [a qualitative picture is

given in Fig. 1a)], causing a larger value of λ than the one predicted by the London equations $\lambda_L = 15.7$ nm. Since the Al bulk coherence length is $\xi_0 = 1.6 \mu\text{m} \gg \lambda_L$, bulk aluminum is in the non-local limit. In the non-local limit, λ is modified by [12]

$$\lambda = 0.65(\lambda_L^2 \xi_0)^{1/3}, \quad (2)$$

which, in the case of aluminum, is $\lambda_{\text{bulk}} = 50$ nm [12, 25]. Thus, bulk aluminum satisfies type-I superconductivity criteria, $\xi_0 > \lambda_{\text{bulk}}$.

However, decreasing the film thickness d eventually decreases the aluminum grain size as well[26], thereby reducing the electron mean free path, l . In this regime, an effective coherence length $\xi < \xi_0$ at $T = 0$ K can be defined [12, 27]

$$\frac{1}{\xi} = \frac{1}{\xi_0} + \frac{1}{l}, \quad (3)$$

which, in the dirty superconductor limit $\xi_0 \gg l$, also modifies λ as

$$\lambda = a \lambda_L \sqrt{\frac{\xi_0}{l}}. \quad (4)$$

a is of order unity which depends on the surface scattering type, being $4/3 \approx 1.33$ for diffusive scattering and $\sqrt{4/3} \approx 1.15$ for specular reflection [8]. Equation (4) is a reasonable approximation, particularly when $l \sim d$. Accordingly, by lowering d , one may reach the regime where $\xi < \lambda$, causing the film to become a type-II superconductor, where the response to external fields is local [see Fig. 1b)]. The transition between superconductivity regimes is determined by the Ginzburg-Landau parameter κ [8]

$$\kappa \equiv \lambda/\xi. \quad (5)$$

Above $\kappa = 1/\sqrt{2}$, the superconductor can be categorized as type-II since the normal-superconductor interface energy becomes negative, thus allowing for the generation of normal paths (vortices) [28]. For thick enough films, κ decreases below $1/\sqrt{2}$ and the film exhibits vortex-free behavior, thus entering the type-I superconductivity regime. By carefully choosing the thicknesses of different thin films, this boundary between superconductivity types occurring at a critical thickness d_c may be attained. In actual thin films, local fluctuations in κ are expected given the disordered nature of the film, thus leading to a spread of values of d_c over which the transition takes place.

For very thin films with thickness in the range of $d \lesssim \lambda$, the response of the film to external perpendicular magnetic fields follows the London equations, reacting with an opposing current \vec{j}_S to an incoming field \vec{A}_S . Since $d \lesssim \lambda$, \vec{A}_S fully penetrates the film. Nevertheless, the expression $\vec{j}_S = -\frac{\mu_0}{\lambda^2} \vec{A}_S$ remains valid [29]. In this scenario, the supercurrent response to \vec{A}_S is the same regardless of the film thickness. However, as thinner films

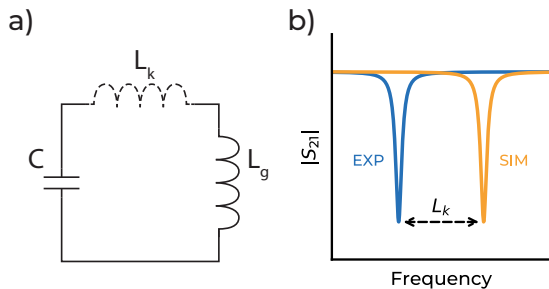


FIG. 2. **a)** LC Resonator equivalent circuit. In the simulations conducted in Sec. IV, no kinetic inductance L_k is considered. In the actual experiment, the contribution from L_k adds to the geometric inductance L_g . **b)** Simulated and experimental resonances are assumed to only deviate due to L_k .

contain a lower amount of charge carriers, Cooper pairs are compelled to attain higher velocities, resulting in a substantial increase in L_k (see Fig. 1d), since $L_k \propto v^2$. The correction to $L_{k,s}$ due to this effect is given by [23]

$$L_{k,s} = \mu_0 \lambda \coth \frac{d}{\lambda} \equiv \mu_0 \lambda_{\text{thin}}, \quad (6)$$

where λ_{thin} represents an effective penetration depth. For $d \gg \lambda$, $\lambda_{\text{thin}} \rightarrow \lambda$, while for $d \ll \lambda$, $\lambda_{\text{thin}} \rightarrow \frac{\lambda^2}{d}$, significantly enhancing $L_{k,s}$. Resonator measurements, as will be detailed in the next section, give direct access to L_k , which can be used to derive λ_{thin} through Eq. (6), and then used to calculate λ .

Finally, λ can be related to the normal metal properties of the thin film as it ultimately depends on the charge carrier properties. Specifically, in the dirty limit with $\xi_0, \lambda \gg l$, λ is related to the normal state resistivity ρ_n of the metal at $T = 0$ K, through [30]

$$\lambda \simeq 105 \text{ nm} \sqrt{\frac{\rho_n (\mu\Omega \cdot \text{cm})}{T_c (\text{K})}}, \quad (7)$$

where T_c is the superconducting critical temperature. Therefore, for each given thickness d , the value of λ estimated through Eq. (6) can be validated against the values of resistance of thin films of the same nominal thickness d .

Equations (6, 7) allow a complete characterization of λ and L_k of thin superconducting films, and are the key expressions used in this work.

III. METHODOLOGIES TO EXTRACT λ

Following the theoretical background presented in Sec. II, two independent approaches are employed to estimate λ for a set of aluminum thin films of varying thickness. The first method involves resonator measurements combined with finite-element simulations, where the effect of λ is reflected in the measured resonance frequency

through changes in L_k . The second approach employs four-probe measurements on resistive devices patterned as meanders.

The resonator measurements allow estimating λ through λ_{thin} [Eq. (6)], while the results of resistance measurements directly lead to λ . Measurement uncertainties derived from fabrication inaccuracies affect both methods differently. Specifically, the discrepancies between nominal and real dimensions are much more subtle in resonators than in four-probe device designs. λ_{thin} is also much more sensitive to deviations in the thickness d . Resistance measurements are, thus, more robust. However, we include resonators in this work as they represent a good benchmark of a real-case scenario where calibrated values of λ are used to predict the values of L_k of a resonator circuit. Therefore, the resistance measurements in this study are in fact used to validate the resonator measurements.

A. Resonance Method

Lumped element LC resonators were chosen for this study in order to achieve a more controlled definition of their inductance L and capacitance C , compared to distributed resonators. LC resonators are characterized by their resonance frequency $\omega = (LC)^{-1/2}$, where C represents the capacitance and $L = L_g + L_k$ is the sum of geometric and kinetic inductances. As explained in Section II, superconductors may exhibit a significantly high L_k , especially for thin films with $d \ll \lambda$.

In order to extract L_k , we first perform an accurate simulation of each resonator studied considering a perfect conductor, thus obtaining L_g and C that lead to a simulated resonance frequency f_{sim} [Fig. 2 a) with $L_k = 0$]. Resonator measurements provide f_{meas} as they contain a total inductance $L = L_g + L_k$ [Fig. 2 a)], so $f_{\text{sim}} > f_{\text{meas}}$. L_k may be then obtained with

$$L_k = L_g \left(\frac{f_{\text{sim}}^2}{f_{\text{meas}}^2} - 1 \right). \quad (8)$$

The L_k obtained in this way determines λ_{thin} using Eq. (6). This method requires a precise simulation of the perfect conductor resonance f_{sim} (see Sec. IV).

B. Resistivity Method

Resistance measurements directly lead to λ through Eq. (7). Since ρ_n is the normal state resistivity at 0 K, it can only be measured by destroying the superconducting state with an external magnetic field. However, the aluminum resistivity is nearly constant at low temperatures, so we instead approximate ρ_n with the value at 4 K.

It is important to note that ρ_n is connected to λ and not to λ_{thin} as in the resonator method. ρ_n and λ are connected through the intrinsic properties of the material, such as the charge carrier mass, the Cooper pair

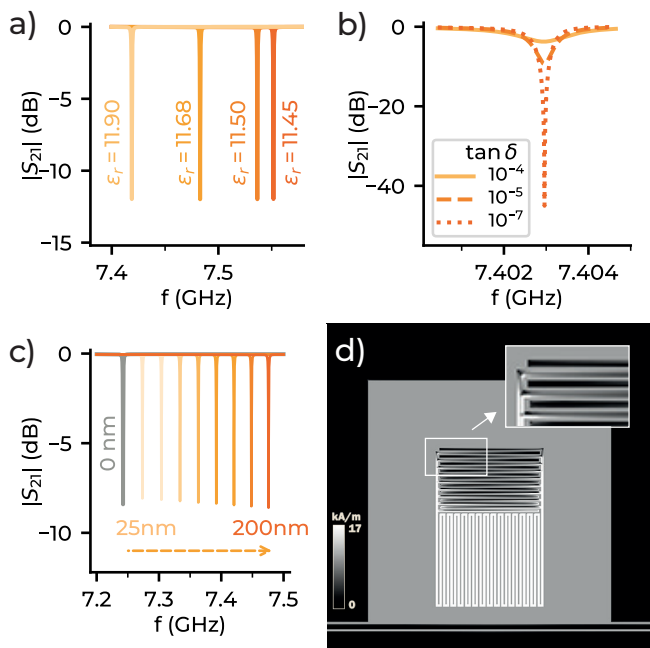


FIG. 3. **a)** LC resonator response with varying Si relative permittivity, ϵ_r . Range of values is typically found in the literature. The actual value used in this work is $\epsilon_r = 11.45$ [31]. **b)** Effect of Si loss tangent, $\tan \delta$, on the quality factor of LC resonators. **c)** Sonnet simulations for an S resonator transmission. Grey curve represents the default response with no thickness. Yellow and increasing saturation color curves correspond to thicknesses ranging from 25 nm to 200 nm. **d)** Simulated current distribution of a LC resonator. The inset shows the current in the last capacitor fingers, where it is minimal.

number density, and the electron mean free path. Accordingly, the thin-film effects described in Eq. (6) do not play a role in the determination of λ through ρ_n .

IV. RESONATOR SIMULATIONS AND DEVICE CHARACTERISTICS

In this section, we summarize the procedure we followed to perform simulations on the resonator circuits, followed by the device characteristics.

For each film thickness d , we employ FastHenry¹ to obtain an estimate of the kinetic inductance fraction $\alpha \equiv L_k/L$. We work in the range $\alpha = 0.02 - 0.5$, as lower α can incur in big inaccuracies in λ , while higher α leads to frequencies lower than our experimental system bandwidth (4 – 8 GHz). These simulations allow us to

¹ We use the version found in <http://www.wrcad.com/ftp/pub/fasthenry-3.0wr-071720.tar.gz> which takes into account the London equations and thus the penetration depth λ in the inductance calculations.

determine the inductor wire width in each resonator for a given d . More details can be found in Appendix C.

Next, we employ Sonnet² to run an entire resonator simulation to obtain the system transmission (see Appendix C for details on the simulations). In these simulations we use the value of the electrical permittivity $\epsilon_r = 11.45$, validated in ref. [31] which was also the low-temperature value confirmed by the manufacturer. As seen in Fig. 3a), the value of the resonance changes noticeably for values of ϵ_r found throughout the literature [32–35], leading to a difference in the obtained λ of up to 100%. Adding realistic values of substrate loss $\tan(\delta)$ to the simulations did not change the resonance frequency appreciably [see Fig. 3b)].

To discern the simulated values of L_g and C we follow the procedure described in ref. [36]. A first simulation of the system yields the resonance frequency f_{sim} . The values of L_g and C are estimated with an additional simulation wherein a known sheet inductance (L_s) is manually incorporated in a single square at the center of the inductor, leading to a modified resonance frequency $f'_{\text{sim}} = 1/(2\pi) \cdot [(L_g + L_s)C]^{-1/2}$. This procedure is equivalent to what is shown in Fig. 2 b), but with a manually incorporated L_k .

However, in actual films a larger thickness d decreases L_g combined with an increase in C . This thickness-dependence effect cannot be directly captured by Sonnet since it is a 2.5D finite-element solver. To obtain the effect of d on L_g and C in the simulation, the thickness is artificially simulated by introducing an additional aluminum layer above the existing structure and connecting both through vias along all edges. For the largest d considered (200 nm) the resulting correction on the resonance frequency amounts to approximately 2% [Fig. 3c)].

Three types of resonators were designed with varying line widths and line gaps to introduce different contributions of L_k . The three designs are defined as small resonators (SR), medium resonators (MR), and large resonators (LR), each with a meander and capacitor widths of 2, 4, and 6 μm , respectively [See Fig. 4a)–d)]. LR are suited for higher L_k contribution while SR are suited for larger thickness.

The lumped description with isolated L and C is justified with the current simulations [Fig. 3d)], where most of the current is present in the meander. Using current simulations as the one shown in Fig. 3d), we estimate that 98% of the energy is located inside the inductor meander. The extra 2% is taken into account to obtain an effective length of the meander for computing the number of squares N in Eq. (1). Moreover, the ground plane is designed sufficiently far from the resonator so we can neglect its contribution to the inductance.

In order to have better statistics in the value of λ for a given thickness, resonators with the same L and different C are designed. This is obtained by changing the last

² <https://www.sonnetsoftware.com/>

fingers of the capacitor, where there is nearly no contribution to L [see inset of Fig. 3d)]. In Fig. 4b) an example of a MR with the last fingers modified is shown. This finger modification reduces C , thus increasing the resonance frequency. The resonators are separated enough in frequency space to be distinguished (> 25 MHz) in the range 7 – 8 GHz.

For the four-probe measurements, a long meander structure was designed [see Fig. 4e) and f)]. Two different meanders were considered, with and without ground plane around the meander. The size of the meander was chosen to ensure that the resistance at 4 K falls within a measurable range of $100 \Omega - 1 \text{ k}\Omega$. A Hall-bar structure has also been used [see Fig. 4 g)] as a complementary measurement of the resistance.

The thicknesses d chosen for the study range from 25 nm to 200 nm. This range includes typical values found for superconducting qubit devices and radiation detectors (50 nm–100 nm). Including this range is indispensable for calibrating λ for real-scenario devices. $d < 50 \text{ nm} \sim \lambda_{\text{bulk,Al}}$ is chosen to observe thin-film effects, while $d > 100 \text{ nm}$ is chosen to explore the regime approaching bulk aluminum behavior. The actual thicknesses were accurately determined using Atomic Force Microscopy.

The devices were fabricated using photolithography on high resistivity silicon wafers. Aluminum was deposited via metal evaporation. The devices were later diced and wirebonded to a ceramic PCB, or to a chip carrier in the case of four-probe devices. More details regarding the fabrication can be found in Appendix B.

Two different evaporators, one Plassys at IFAE and another from Univex at CNM, were used in this study in order to account for possible fabrication dependencies on λ . While the IFAE evaporator is only used for aluminum, the CNM evaporator contains other metals and may thus lead to a higher amount of impurities.

Altogether, the different variety of designs and fabrication conditions account for potential systematic errors on λ , ensuring a more comprehensive analysis.

V. EXPERIMENT

All devices were mounted in a sample holder at the mixing chamber plate of a dilution refrigerator ($T = 20 \text{ mK}$) and subjected to measurements using a Vector Network Analyzer (VNA) at power levels near the single photon regime. Full setup schematics can be found in Appendix A. 4-probe structures were either located in the same chip as the resonators or in a separate chip, in which case they were located either at the mixing chamber or at the still plate of the dilution fridge.

Resistance measurements were performed at room temperature and at 4 K [see Fig. 5 d)]. Then, a continuous measurement was run at a low current while sweeping the temperature around $T_{C,\text{bulk}} \sim 1.2 \text{ K}$ to find the critical temperature of the sample. T_C was determined at the

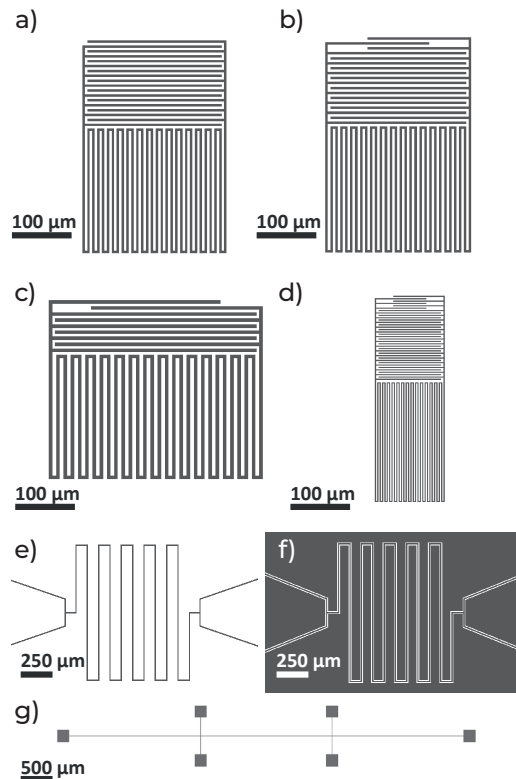


FIG. 4. LC resonator device design variations: (a) medium (MR); (b) medium with adjusted finger capacitor; (c) large (LR), (d) and small (SR). Design of a 4-probe measurement meander without (e) and with (f) surrounding ground plane. (g) Layout of a Hall-bar measurement.

midpoint of the superconductor-normal transition where the resistance dropped by 50%. A typical resonator measurement is shown in Fig. 5c) for two different resonator thicknesses.

The resonator response was fit to the following expression [37]

$$S_{21} = ae^{i\alpha} e^{-2\pi i f \tau} \left[1 - \frac{(Q_l/|Q_c|)e^{i\phi}}{1 + 2iQ_l(f/f_r - 1)} \right], \quad (9)$$

where the factor between brackets is the actual resonator response, while the pre-factor in front accounts for the response of the rest of the circuit. a is an attenuation constant, α represents a phase shift and τ is the electrical delay of the measurement line. Q_l is the loaded quality factor related to the complex coupling quality factor Q_c and internal quality factor Q_i , through $Q_l^{-1} = Q_i^{-1} + \text{Re}(Q_c^{-1})$. Finally, ϕ expresses the impedance mismatch, and f_r is the resonator frequency. Typical fits to the resonator response are shown in Fig. 6, where one can see that the impedance mismatch is correctly captured.

Our fitting process follows from a routine inspired by ref. [37]. In that study, the data fitting is performed sequentially, until the full expression for S_{21} is obtained. However, with such a sequential process it is hard to propagate errors in the fitting, and correlations between

TABLE I. Results of the fits from Fig. 6. All parameters are used in Eq. 9 to fit the resonator response. Parameter uncertainties are obtained using the iminuit software, as explained in the main text.

Res. ID	f_r (GHz)	δf_r (kHz)	$ Q_c $	$\delta Q_c $	Q_l	δQ_l	ϕ	$\delta\phi$	α	$\delta\alpha$	a	δa	τ (Hz)	$\delta\tau$ (Hz)
0	7.0056	8	$1.52 \cdot 10^4$	$3 \cdot 10^2$	$9.2 \cdot 10^3$	200	0.22	0.02	-3.78	0.04	$1.01 \cdot 10^{-3}$	$3 \cdot 10^{-6}$	$6.97 \cdot 10^{-8}$	$7 \cdot 10^{-11}$
1	7.0115	1	$3.47 \cdot 10^3$	2	$4.2 \cdot 10^3$	3	-0.76	0.001	-2.87	0.001	$8.17 \cdot 10^{-3}$	$1 \cdot 10^{-6}$	$6.99 \cdot 10^{-8}$	$5 \cdot 10^{-14}$

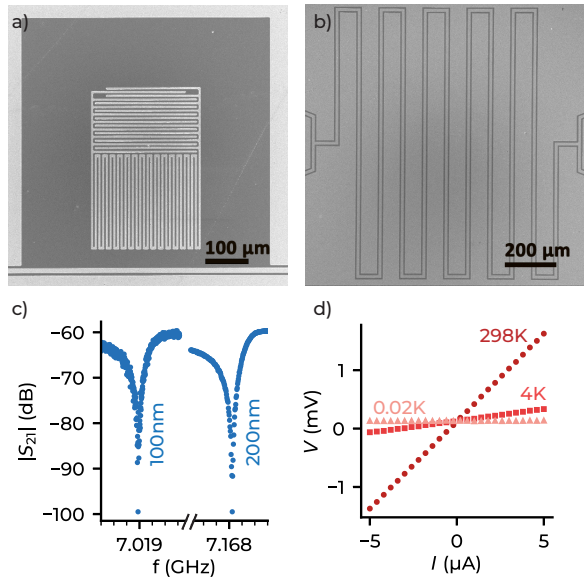


FIG. 5. **a)** Scanning electron micrograph (SEM) of a LC resonator. **b)** SEM of a 4-probe meander. **c)** S_{21} data and fit of measured resonators with 100 nm and 200 nm thickness. Each minor tick corresponds to 1 MHz **d)** Resistance measurements at room temperature (RT), 4 K and 10 mK.

parameters are lost. For that reason, we use the sequential procedure to yield our initial parameter guess. Standard scipy optimization routines are employed for this method. Once an initial set of parameters is obtained, we use the iminuit library [38] for fitting the full S_{21} expression. Iminuit is a library mainly used in the particle physics community, with a focus on error propagation and accurate uncertainty estimation. The S_{21} fit has seven parameters, which makes it a complex fit, and proper error estimation becomes relevant. In most fits the initial guess and final fitting parameters were close. In general, having good initial parameters for iminuit is indispensable. In some resonators, however, iminuit fitting found a considerably better solution than the initial one, while providing a correct error estimation.

Table I shows fitted parameters from resonators in Fig. 6, with the corresponding errors. The error in frequency δf_r is of order 10^{-6} , which is the most important parameter to extract λ . The resonator internal quality factor Q_i is not used in this study. In fact, the resonators in this work are designed with $Q_l \ll Q_i$ to maximize the signal strength, and therefore Q_i is not very accurately

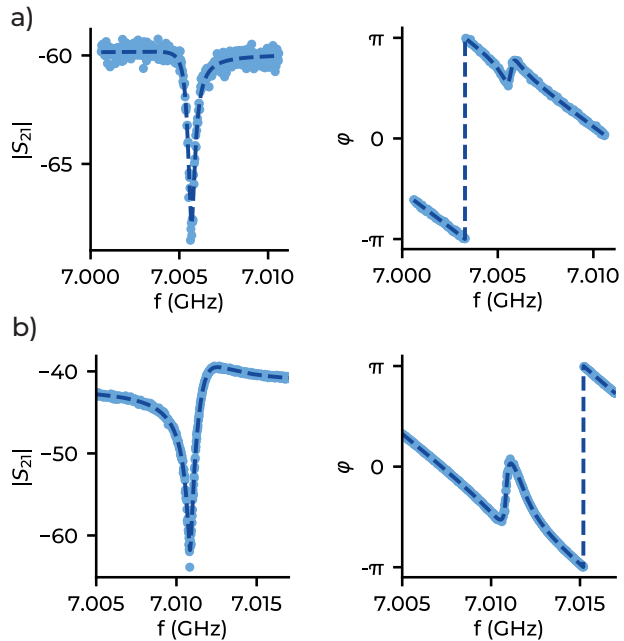


FIG. 6. S_{21} resonator response in magnitude ($|S_{21}|$, left) and phase (φ , right). The fit using our procedure is superimposed to the light blue data points as a dark blue dashed line. **a)** 100 nm-thick MR resonator. **b)** 200 nm-thick MR resonator, with the same design as the device in **a)**.

determined, lying in the range 50.000-100.000 showing no obvious thickness dependence.

VI. RESULTS

The obtained values of λ for each sample thickness d from both resonator and resistance measurements are plotted in Fig. 7. Each point of the resonator measurement consists of an average of several resonators on the same chip with varying capacitance and kinetic inductance ratio (see Table II), as explained in Sec. IV. The vertical error bars correspond to the standard error of the mean, which is smaller than the marker size. The error in the horizontal axis corresponds to the uncertainty in AFM measurements to determine the actual film thickness. The resistance measurements consist of a single structure in each device, given the small error in the fitting of the resistance [Fig. 5].

Table II shows the full experimental results obtained for both the resonance and resistance measurements. A

TABLE II. Results for both resistance and resonance frequency measurements. d_{nom} is the nominal target thickness, while d_{meas} is the measured thickness using atomic force microscopy. λ is the measured average penetration depth. Measurement type is “LC” for lumped resonators and “R” for 4-probe resistance measurements. “N” represents the number of devices measured for each particular thickness, which include small resonators (SR), medium resonators (MR), and large resonators (LR) for the resonance frequency measurements, and four-probe (4P) and Hall bar (HB) for the resistance measurements. The fabrication facility is specified for each device. For resonator measurements, λ_{thin} is shown, together with surface kinetic inductance $L_{k,s}$. For resistance measurements, residual-resistance ratio, defined as $RRR = R_{\text{RT}}/R_{\text{AK}}$ is shown.

Device id	d_{nom} (nm)	d_{meas} (nm)	λ (nm)	Meas.	Design	N	Fab.	λ_{thin} (nm)	$L_{k,s}$ (fH)
1	25	28 ± 4	163.3 ± 0.4	LC	MR	9	IFAE	965 ± 4	1212 ± 5
3	50	52 ± 2	118.3 ± 0.3	LC	MR	9	IFAE	286 ± 1	359 ± 2
4	75	73 ± 2	94.3 ± 0.6	LC	MR	5	IFAE	145 ± 2	182 ± 3
6	75	78 ± 3	97.2 ± 0.9	LC	LR	9	IFAE	145 ± 2	182 ± 3
8	100	105 ± 2	76.2 ± 0.9	LC	MR	5	IFAE	87 ± 2	109 ± 3
9	100	105 ± 2	62.6 ± 0.2	LC	LR	5	IFAE	67 ± 2	84 ± 3
12	100	127 ± 5	63.3 ± 1.1	LC	SR	9	CNM	66 ± 1	83 ± 2
14	200	188 ± 3	58.1 ± 1.1	LC	MR	5	IFAE	58 ± 1	73 ± 2
16	200	207 ± 5	58.8 ± 1.0	LC	MR	6	CNM	59 ± 1	74 ± 2

Device id	d_{nom} (nm)	d_{meas} (nm)	λ (nm)	Meas.	Design	N	Fab.	RRR	T_C (K)
2	25	28 ± 4	162.9 ± 1.2	R	4P	1	IFAE	2.1 ± 0.1	1.32 ± 0.03
5	75	76 ± 3	84.1 ± 0.7	R	4P	1	CNM	4.8 ± 0.1	1.22 ± 0.01
7	100	97 ± 3	80.6 ± 0.7	R	4P	1	CNM	6.1 ± 0.1	1.27 ± 0.02
10	100	105 ± 2	69.4 ± 0.6	R	4P	1	IFAE	7.2 ± 0.1	-
11	100	105 ± 2	68.7 ± 0.6	R	HB	1	IFAE	7.2 ± 0.1	-
13	100	127 ± 5	66.0 ± 0.6	R	4P	1	CNM	7.4 ± 0.1	1.20 ± 0.05
15	200	188 ± 3	55.3 ± 0.5	R	4P	1	IFAE	11.6 ± 0.1	1.20 ± 0.02
17	200	207 ± 5	53.6 ± 0.4	R	4P	1	CNM	9.9 ± 0.1	1.20 ± 0.05

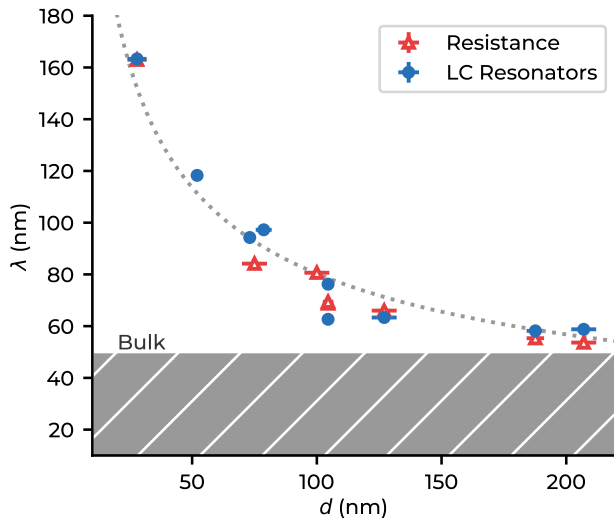


FIG. 7. Estimated penetration depth λ as function of device thickness d . Two measurement methods are shown: resistance measurements (red triangles) and LC resonator resonances (blue circles). Bulk penetration depth is shown as a lower limit. The thickness of samples is measured using atomic force microscopy. The fitting curve is $\lambda = a\lambda_L(\xi_0/d)^{1/2}$ using Eqs. (3, 4) and assuming the electron mean-free path to be $l = d$. The fitted parameter is $a = 1.28 \pm 0.03$, half way between specular and diffusive scattering.

total of 70 structures have been analyzed, combining the

two measurement methods (see Sec. III), three different designs for each measurement method, along with eight different thicknesses and two evaporation facilities. This combination reduces considerably the possibility of a systematic error on the experiment, and provides a good statistical ensemble from which to extract conclusive values of λ .

The data in Fig. 7 exhibit a consistent trend, with λ increasing rapidly for $d < 100$ nm and approaching bulk values for $d \sim 200$ nm, validating the chosen thickness range. For very low thicknesses, it is common to assume that the electron mean-free path l is limited by surface scattering, leading to $l = d$ [8]. With this assumption, λ can be fitted to Eq. (4) leaving a as a fitting parameter. The fit yields $a = 1.26 \pm 0.03$, which lies in a regime of mixed scattering. It is important to note that Eq. (4) is only valid in the regime of a type-II superconductor, as the limit for large l is λ_L , and not λ_{bulk} . Using the fitted curve, $\lambda = \lambda_{\text{bulk}}$ at $d \simeq 250$ nm, which sets this thickness as an upper limit to the validity of the expression.

The resonance frequency method gives access to L_k through Eq. (8), which is then converted to $L_{k,s}$ via Eq. (1). $L_{k,s}$ is proportional to λ_{thin} , and both are shown in Fig. 8a). In this figure, only LC resonators are plotted, and the exponential increase at low thicknesses is more pronounced than the increase of λ in Fig. 7, as expected. Large $L_{k,s}$ values near ~ 10 pF are predicted for aluminum with $d \sim 10$ nm. Combined with a long enough meander, pure aluminum can attain L_k values comparable to those exhibited by superconductors [39].

Figure 8b) and c) show variations on the design and

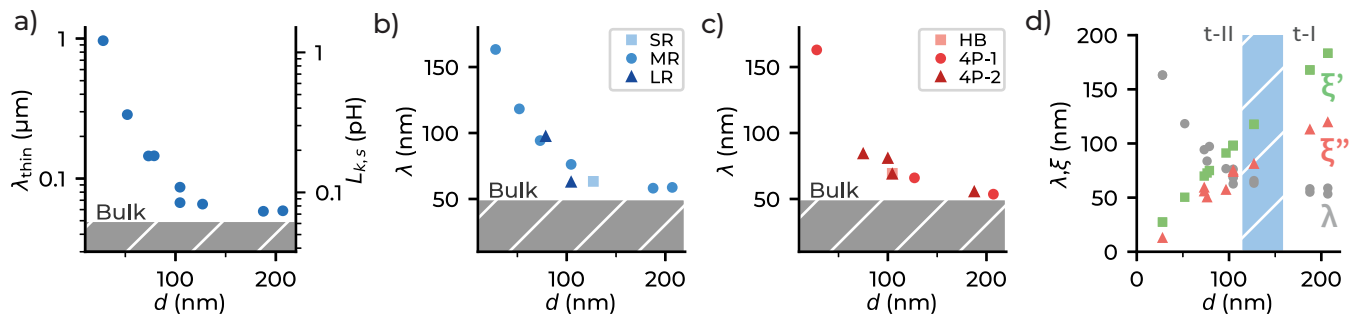


FIG. 8. **a)** LC resonator response, plotted in two scales: λ_{thin} (left y-axis) and L_k (right y-axis), which are proportional, see Eq. (6). **b)** Measured λ by the resonance frequency method for different thicknesses. Different resonator types are shown. The devices fabricated in CNM evaporator are highlighted. **c)** Measured λ using the resistance method for different thicknesses. Different resistance structures are shown, the two types of four-probe, with (1) and without (2) ground plane, and the Hall bar. The devices fabricated in CNM evaporator are highlighted. **d)** Estimated dependence of coherence length ξ on thickness using the fit from Fig. 7. ξ' is calculated assuming $l = d$ with Eq (3). According to this fit, the transition between superconductivity regimes, when $\xi/\lambda = \sqrt{2}$ [28], occurs at a critical thickness $d_c \simeq 113$ nm. ξ'' is calculated from l obtained from the relation $\rho \cdot l = 4 \cdot 10^{-12} \Omega \cdot \text{cm}^2$. The blue region is the predicted zone where d_c could fall according to these two methods.

deposition system for both resonance and resistance measurements, respectively. In Fig. 8b), λ from the three different resonator designs are shown. The devices fabricated at the different fabrication facilities do follow the overall trend, considering the differences in the two deposition systems. The noticeable difference at $d = 100$ nm may arise from a systematic difference in the device geometry between M and L resonators not accounted for.

Resistance measurements are displayed in Fig. 8 c). All values follow a consistent trend $\lambda \sim 1/\sqrt{d}$. Most data are obtained from 4-probe structures with (4P-1) and without (4P-2) surrounding ground plane. The single Hall bar value is consistent with a 4-probe measurement. Devices fabricated at different fabrication facilities did not show visible deviations in λ despite the difference in the residual resistance ratio RRR values (Table II).

The results obtained in this work allow us to provide estimates of the critical thickness d_c where aluminum turns from a type-I to a type-II superconductor. Such a transition is expected to occur for a value of $\kappa = 1/\sqrt{2}$ in Eq. (5) [28]. In Fig. 8d), the values of λ obtained are compared to values of ξ obtained from two different assumptions on the dependence of the electron mean-free path l as function of thickness d . Our first method assumes $l = d$, which is a reasonable approximation for thin films as already argued, leading to a value ξ' estimated from Eq. (3). The thickness that satisfies $\xi = \sqrt{2}\lambda$ is $d_c^{(1)} \simeq 113$ nm. It is important to note that this fit, which assumes a linear dependence between d and l , fails for large d . An alternative method to predict ξ is obtained by using the relation [40, 41] $\rho \cdot l = 4 \cdot 10^{-12} \Omega \cdot \text{cm}^2$ known for aluminum. According to this relation, a different ξ'' is obtained through Eq. (3) and the ρ values obtained from the meanders, leading to $d_c^{(2)} \simeq 155$ nm. In either case, an exact description of l as function of d is outside of the scope of this work. Therefore our assumptions allow us to define a region of critical thick-

nesses $d_c = 113 \text{ nm} - 155 \text{ nm}$ where the transition between superconductivity types may occur. As argued in Sec. II, the actual transition between superconductivity types may take place over a certain range of values of d_c , given the intrinsic inhomogeneity of κ due to the disordered nature of thin films. In summary, our results suggest that the thicker samples ($d > 150$ nm) may enter the regime towards type-I superconductivity [40], unlike the thinner ones ($d < 50$ nm) which are more likely to behave as type-II local superconductors.

VII. CONCLUSIONS

In this work, we performed a characterization of the magnetic penetration depth λ in superconducting aluminum for thicknesses in the range 25 nm–200 nm. The values of λ obtained range from 163.3 nm for the thinnest samples down to 53.6 nm, approaching the aluminum bulk value for the thickest films. Our measurements of λ as function of thickness represent a guide to circuit designs where inductance plays a significant role, such as, e.g., circuit QED and kinetic inductance detectors.

We have also introduced an accurate fitting procedure for resonators which can easily be extended to other experimental settings. For simultaneous parameter fits, sequential fitting can be a good process to obtain each parameter at a time. However, this process does not provide a good estimation of the fitting error and the correlations between parameters. Using the result of sequential fitting as the initial guess, we then fitted with the `iminuit` package, providing an accurate error estimation and, in particular instances, a better parameter prediction.

Our work has also enabled us to provide an estimation of the thickness range at which thin-film aluminum starts behaving as a type-I superconductor. Further work is needed to explore the actual transition point and in-

investigate potential new circuit functionalities in thicker aluminum films such as quasiparticle traps using the dependence of the superconducting gap on thickness [42, 43] or the exclusion of vortices in thick enough films.

ACKNOWLEDGEMENTS

We would like to give special thanks to Sonnet support software for their help in running our simulations. We also want to thank Qilimanjaro engineers David Eslava and Yifei Chen for their collaboration and help during measurements, and Prof. Teun Klapwijk and Prof. Teresa Puig for their insightful comments. D. L.-N. ac-

knowledges support by an FPI grant from the Spanish Ministry of Science and Innovation (MICIN). We also acknowledge funding from the Ministry of Economy and Competitiveness and Agencia Estatal de Investigación (RYC2019-028482- I, PCI2019-111838-2, PID2021-122140NB-C31), the European Commission (FET-Open AVaQus GA 899561, QuantERA), and program ‘Doctorat Industrial’ of the Agency for Management of University and Research Grants (2020 DI 41; 2020 DI 42). IFAE is partially funded by the CERCA program of the Generalitat de Catalunya. This study was supported by MICIN with funding from European Union NextGenerationEU(PRTR-C17.I1) and by Generalitat de Catalunya.

-
- [1] J. F. Cochran, D. E. Mapother, and R. E. Mould, “Superconducting transition in aluminum,” *Phys. Rev.*, vol. 103, pp. 1657–1669, Sep 1956.
 - [2] M. Brooks, “Quantum computers: what are they good for?,” *Nature*, vol. 617, pp. S1–S3, May 2023.
 - [3] Y. Kim, A. Eddins, S. Anand, K. Wei, E. Berg, S. Rosenblatt, H. Nayfeh, Y. Wu, M. Zaletel, K. Temme, and A. Kandala, “Evidence for the utility of quantum computing before fault tolerance,” *Nature*, vol. 618, pp. 500–505, 06 2023.
 - [4] A. Blais, A. L. Grimsmo, S. M. Girvin, and A. Wallraff, “Circuit quantum electrodynamics,” *Rev. Mod. Phys.*, vol. 93, p. 025005, May 2021.
 - [5] A. Pérez-Salinas, D. López-Núñez, A. García-Sáez, P. Forn-Díaz, and J. I. Latorre, “One qubit as a universal approximant,” *Phys. Rev. A*, vol. 104, p. 012405, Jul 2021.
 - [6] G. Coiffard, M. Daal, N. Zobrist, N. Swimmer, S. Steiger, B. Bumble, and B. A. Mazin, “Characterization of sputtered hafnium thin films for high quality factor microwave kinetic inductance detectors,” *Superconductor Science and Technology*, vol. 33, p. 07LT02, may 2020.
 - [7] I. Nsanzineza and B. Plourde, “Trapping a single vortex and reducing quasiparticles in a superconducting resonator,” *Physical Review Letters*, vol. 113, sep 2014.
 - [8] M. Tinkham, *Introduction to Superconductivity*. Dover Books on Physics Series, Dover Publications, 2004.
 - [9] K. Watanabe, K. Yoshida, and T. A. Kohjiro, “Kinetic inductance of superconducting coplanar waveguides,” *Japanese Journal of Applied Physics*, vol. 33, p. 5708, oct 1994.
 - [10] P. Forn-Díaz, J. Lisenfeld, D. Marcos, J. J. García-Ripoll, E. Solano, C. J. P. M. Harmans, and J. E. Mooij, “Observation of the bloch-siegert shift in a qubit-oscillator system in the ultrastrong coupling regime,” *Phys. Rev. Lett.*, vol. 105, p. 237001, Nov 2010.
 - [11] S. J. Weber, G. O. Samach, D. Hover, S. Gustavsson, D. K. Kim, A. Melville, D. Rosenberg, A. P. Sears, F. Yan, J. L. Yoder, W. D. Oliver, and A. J. Kerman, “Coherent coupled qubits for quantum annealing,” *Phys. Rev. Appl.*, vol. 8, p. 014004, Jul 2017.
 - [12] P. G. D. Gennes, *Superconductivity of Metals and Alloys*. CRC Press, Mar. 2018.
 - [13] A. F. Mayadas, “Intrinsic Resistivity and Electron Mean Free Path in Aluminum Films,” *Journal of Applied Physics*, vol. 39, pp. 4241–4245, 11 2003.
 - [14] A. F. Mayadas, R. Feder, and R. Rosenberg, “Resistivity and Structure of Evaporated Aluminum Films,” *Journal of Vacuum Science and Technology*, vol. 6, pp. 690–693, 07 1969.
 - [15] A. F. Mayadas and M. Shatzkes, “Electrical-resistivity model for polycrystalline films: the case of arbitrary reflection at external surfaces,” *Phys. Rev. B*, vol. 1, pp. 1382–1389, Feb 1970.
 - [16] A. I. Gubin, K. S. Il’in, S. A. Vitusevich, M. Siegel, and N. Klein, “Dependence of magnetic penetration depth on the thickness of superconducting nb thin films,” *Phys. Rev. B*, vol. 72, p. 064503, Aug 2005.
 - [17] K. Yoshida, K. Watanabe, T. Kisu, and K. Enpuku, “Evaluation of magnetic penetration depth and surface resistance of superconducting thin films using coplanar waveguides,” *IEEE Transactions on Applied Superconductivity*, vol. 5, no. 2, pp. 1979–1982, 1995.
 - [18] H. Rotzinger, S. T. Skacel, M. Pfirrmann, J. N. Voss, J. Münzberg, S. Probst, P. Bushev, M. P. Weides, A. V. Ustinov, and J. E. Mooij, “Aluminium-oxide wires for superconducting high kinetic inductance circuits,” *Superconductor Science and Technology*, vol. 30, p. 025002, nov 2016.
 - [19] J. Bylander, S. Gustavsson, F. Yan, F. Yoshihara, K. Harrabi, G. Fitch, D. G. Cory, Y. Nakamura, J.-S. Tsai, and W. D. Oliver, “Noise spectroscopy through dynamical decoupling with a superconducting flux qubit,” *Nature Physics*, vol. 7, pp. 565–570, May 2011.
 - [20] C. Wang, Y. Y. Gao, I. M. Pop, U. Vool, C. Axline, T. Brecht, R. W. Heeres, L. Frunzio, M. H. Devoret, G. Catelani, L. I. Glazman, and R. J. Schoelkopf, “Measurement and control of quasiparticle dynamics in a superconducting qubit,” *Nature Communications*, vol. 5, no. 1, p. 5836, 2014.
 - [21] A. B. Pippard and W. L. Bragg, “An experimental and theoretical study of the relation between magnetic field and current in a superconductor,” *Proceedings of the Royal Society of London. Series A. Mathematical and Physical Sciences*, vol. 216, no. 1127, pp. 547–568, 1953.
 - [22] D. C. Mattis and J. Bardeen, “Theory of the anomalous skin effect in normal and superconducting metals,” *Phys.*

- Rev.*, vol. 111, pp. 412–417, Jul 1958.
- [23] R. L. Kautz, “Picosecond pulses on superconducting striplines,” *Journal of Applied Physics*, vol. 49, pp. 308–314, 08 2008.
- [24] J. P. Turneaure, J. Halbritter, and H. A. Schwettman, “The surface impedance of superconductors and normal conductors: The Mattis-Bardeen theory,” *Journal of Superconductivity*, vol. 4, pp. 341–355, 1991.
- [25] T. E. Faber and A. B. Pippard, “The penetration depth and high-frequency resistance of superconducting aluminium,” *Proceedings of the Royal Society of London. Series A. Mathematical and Physical Sciences*, vol. 231, pp. 336–353, Sept. 1955.
- [26] R. H. Meservey and P. M. Tedrow, “Properties of very thin aluminum films,” *Journal of Applied Physics*, vol. 42, pp. 51–53, 1971.
- [27] D. Saint-James, G. Sarma, E. J. Thomas, and P. Silverman, *Type II superconductivity*. Pergamon, New York, 1969.
- [28] A. A. Abrikosov, “Magnetic properties of superconductors of the second group,” *Sov. Phys. - JETP (Engl. Transl.); (United States)*, 1957.
- [29] J. Pearl, “Current distribution in superconducting films carrying quantized fluxoids,” *Applied Physics Letters*, vol. 5, pp. 65–66, 11 2004.
- [30] R. R. Hake, “Paramagnetic superconductivity in extreme type-II superconductors,” *Phys. Rev.*, vol. 158, pp. 356–376, Jun 1967.
- [31] J. Krupka, J. Breeze, A. Centeno, N. Alford, T. Claussen, and L. Jensen, “Measurements of permittivity, dielectric loss tangent, and resistivity of float-zone silicon at microwave frequencies,” *IEEE Transactions on Microwave Theory and Techniques*, vol. 54, no. 11, pp. 3995–4001, 2006.
- [32] A. Bruno, G. de Lange, S. Asaad, K. L. van der Enden, N. K. Langford, and L. DiCarlo, “Reducing intrinsic loss in superconducting resonators by surface treatment and deep etching of silicon substrates,” *Applied Physics Letters*, vol. 106, p. 182601, 05 2015.
- [33] M. Göppl, A. Fragner, M. Baur, R. Bianchetti, S. Filipp, J. M. Fink, P. J. Leek, G. Puebla, L. Steffen, and A. Wallraff, “Coplanar waveguide resonators for circuit quantum electrodynamics,” *Journal of Applied Physics*, vol. 104, p. 113904, 12 2008.
- [34] D. S. Christoforus, G. Andrew, M. I. K, and P. J. P, “Electromagnetic simulation and microwave circuit approach of heat transport in superconducting qubits,” *Journal of Physics Communications*, vol. 7, no. 1, p. 015005, 2023.
- [35] S. J. Weber, K. W. Murch, D. H. Slichter, R. Vijay, and I. Siddiqi, “Single crystal silicon capacitors with low microwave loss in the single photon regime,” *Applied Physics Letters*, vol. 98, p. 172510, 04 2011.
- [36] S. Doyle, P. D. Mauskopf, J. A. Naylon, A. Porch, and C. Duncombe, “Lumped element kinetic inductance detectors,” *Journal of Low Temperature Physics*, vol. 151, pp. 530–536, 2008.
- [37] S. Probst, F. B. Song, P. A. Bushev, A. V. Ustinov, and M. Weides, “Efficient and robust analysis of complex scattering data under noise in microwave resonators,” *Review of Scientific Instruments*, vol. 86, feb 2015.
- [38] H. Dembinski and P. O. et al., “scikit-hep/iminuit,” Dec 2020.
- [39] N. Maleeva, L. Grünhaupt, T. Klein, F. Levy-Bertrand, O. Dupre, M. Calvo, F. Valenti, P. Winkel, F. Friedrich, W. Wernsdorfer, *et al.*, “Circuit quantum electrodynamics of granular aluminum resonators,” *Nature communications*, vol. 9, no. 1, p. 3889, 2018.
- [40] B. L. Brandt, R. D. Parks, and R. D. Chaudhari, “Intermediate state of thin superconductors,” *Journal of Low Temperature Physics*, vol. 4, no. 1, pp. 41–63, 1971.
- [41] J. Romijn, T. M. Klapwijk, M. J. Renne, and J. E. Mooij, “Critical pair-breaking current in superconducting aluminum strips far below T_c ,” *Phys. Rev. B*, vol. 26, pp. 3648–3655, Oct 1982.
- [42] X. Pan, Y. Zhou, H. Yuan, L. Nie, W. Wei, L. Zhang, J. Li, S. Liu, Z. H. Jiang, G. Catelani, L. Hu, F. Yan, and D. Yu, “Engineering superconducting qubits to reduce quasiparticles and charge noise,” *Nature Communications*, vol. 13, no. 1, p. 7196, 2022.
- [43] K. Li, S. K. Dutta, Z. Steffen, D. Poppert, S. Keshvari, J. Bowser, B. S. Palmer, C. J. Lobb, and F. C. Wellstood, “Long-lived transmons with different electrode layouts,” *MRS Advances*, vol. 7, no. 13, pp. 273–277, 2022.

Appendix A: Experimental Setup

The experimental setup used in the measurements of all devices presented in this work is shown in Fig. 9.

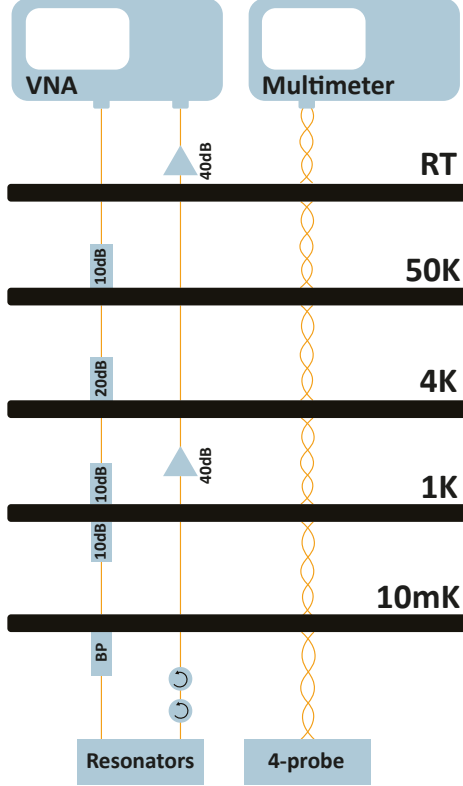


FIG. 9. Measurement setup. High-frequency coaxial lines are attenuated 50dB and filtered above 8 GHz. The output signal is passed through two circulators and amplified through a HEMT amplifier and a room temperature amplifier. Resonators were measured with an Agilent Vector Network Analyzer E5071B. DC lines for resistance measurement were twisted pairs thermalized in several stages at the refrigerator. A Keithley 2600B source measurement unit was used for these measurements.

Appendix B: Fabrication

High resistivity silicon wafers from TOPSIL provider are used as substrates for all the fabricated device. The basic processing steps for patterning the electronic devices are as follows.

Samples are diced in quarter wafers and subsequently cleaned in acetone, rinsed in isopropanol and blown dry in N_2 stream. Substrates are dehydrated before photoresist deposition. LOR3A plus AZ6512 resists are spin coated and soft baked sequentially. A Karl Suss mask aligner is used for resist-stack exposure and then a standardized

development sequence is applied. The pattern transfer consists in aluminum thin film deposition followed by a lift off of the resist in NMP solvent. The aluminum deposition was performed by e-beam evaporation for the given thicknesses. The remaining LOR3A is removed by mild oxygen plasma treatment. For electrical characterization, the samples were diced appropriately and mounted onto ceramic PCBs. Devices were wire-bonded with aluminum wires to either a sample holder for AC measurements or to chip carriers for DC measurements. Exemplary images of actual devices are shown in Figs. 5 a) and b).

Appendix C: Simulations

FastHenry simulations were used to obtain an approximation of the kinetic inductance fractions of the resonator inductances, $\alpha \equiv L_k/L$. Those simulations determine the width and gap of the meanders, along with the number of meander turns. A schematic design is shown in Fig. 10 a).

For FastHenry simulations, the value of λ had to be estimated, since it is needed for estimating the kinetic inductance L_k . We fitted a phenomenological behaviour of λ as a decaying exponential with limiting value $\lambda_{\text{bulk}} = 50$ nm for large thicknesses, together known values from previous internal studies at $d = 25$ nm and $d = 50$ nm (see Fig. 10b)). The used expression is

$$\lambda(d)[\text{nm}] = \lambda_{\text{bulk}} + 196 \cdot e^{-d[\text{nm}]/74.3}. \quad (\text{C1})$$

The resulting simulations show $\alpha = 0.47$ for 25 nm thickness, and $\alpha = 0.03$ for 200 nm, both inside the limits set for our work. These results correspond to M resonator, while L and S resonator designs are intended for lower and higher thickness, respectively, so they deviate in the opposite limits.

The main simulations were run with Sonnet, with 1 μm fine meshing. To have different resonators with different resonance frequency but the same value of L_k , only the last capacitor fingers were modified (see Fig. 10c)), as the current in these last fingers is minimal, thus the resistivity could be kept constant (see main text Fig. 3d)). This was easily achieved by parameterizing a Sonnet file and sweeping over the length of the last fingers. The values were almost evenly spaced. The number of fingers modified and the distance was different for each resonator type (M, S and L). Simulations for M resonators are shown in Fig. 10d).

When performing the simulation of a given resonator, not only the resonance frequency f_0 was acquired, but also the inductance, L , and capacitance, C . We followed the method described by Doyle [36], which consists on adding an extra known sheet inductance in a single square of the meander and obtaining a new modified frequency f'_0 . Together with f_0 and the known inductance value, L and C can be separately obtained. More details can be found in the main text Section III A.

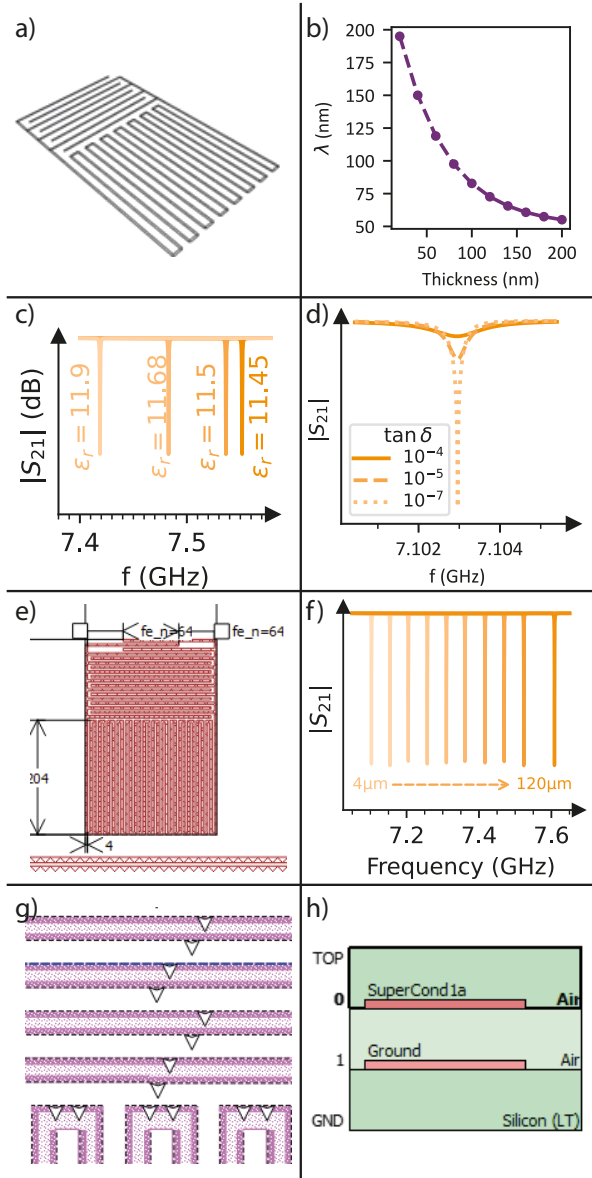


FIG. 10. **a)** FastHenry modelization of the resonator. The number of fingers and meanders, along with widths and thicknesses, were variable parameters. **b)** The dash-dotted line represents the estimated values of the penetration depth used in the simulations, using previous internal results and the bulk value. **c)** Sonnet picture of a simulated resonator. Only last three fingers (of M resonators) are changed to modify the resonator frequency. The finger lengths range from $4 \mu\text{m}$ to $120 \mu\text{m}$. **d)** Simulated resonator frequencies by modifying the spacing in the last fingers of the resonator. Resonances are separated $30 - 50$ MHz, enough to be distinguishable in the experiment. **e)** Zoom of the simulation design with the through via used represented as white triangles in the fingers (upper wires) and meanders (bottom turning wires) to connect the two layers of metal used to emulate thickness. **f)** Sonnet layers, where two metallic layers are placed to simulate the film thickness.

Finally, we need to add the thickness into the simu-

lation, otherwise the predicted value of λ could be even negative. The simulation design we developed which includes the vertical dimension can be seen in Fig. 10e-f). Two layers of superconductor are added on top of the silicon, separated by a distance d . Then, these two layers are connected through vias along all the edges. This effectively creates a thick resonator, reducing the inductance and increasing the capacitance.

As shown in main text [Fig. 3c)], the difference between sheet metal (gray resonance) and the thickest sample ($200 \mu\text{m}$) was around 2%, comparable to the difference added due to L_k in real experiments for thicker samples, thus being extremely important.

These thick simulations required a significant amount of computer memory. Instead of simulating all the resonators with all the different finger lengths, we only simulated the resonators with the lowest and largest last fingers length and compared the difference with their respective sheet resonators with no thickness. For these two extreme cases, the ratios of the simulated frequencies obtained between the purely 2-dimensional and the thick capacitance and inductances were the same up to $< 0.1\%$, so we applied this ratio to all the 2-dimensional resonators obtained with simulations without including the thickness to obtain the corresponding thick-device value.

Appendix D: Data Fitting

The main procedure to fit the data using the `iminuit` package is already detailed in Sec. V. Using `iminuit` one has access to the correlation matrix between variables, which is defined as

$$\rho_{ij} = \frac{\sigma_{ij}}{\sqrt{\sigma_{ii}\sigma_{jj}}}. \quad (\text{D1})$$

Here, σ_{ii} is the variance of variable i , and σ_{ij} is the covariance between variables i and j , if $i \neq j$.

When using the fitting formula for the transmission measurements S_{21} Eq. (9), both quality factors, Q_L and $|Q_c|$, show high correlation and, indeed, Q_L is bounded by Q_c . Other variables that are highly correlated are f_r with ϕ_0 . α and τ are instead fully correlated, given that both appear in the exponential pre-factor of S_{21} . In both cases, a slight change in one of them, provokes adaptations in the other coupled variable to minimize the cost function, which indicates correlation. One could, in principle, parameterize the model in an alternative way to Eq. (9) to use purely independent variables. However, this parameterization will probably require the use of variables with little physical meaning, thus losing the benefits and information obtained from fitting the variables with actual physical meaning.

In Table III, correlations between parameters are shown for resonator in Fig. 6a).

TABLE III. Table with correlation for fitting of resonator on Fig. 6a). Parameters can be seen in Eq. (9).

	a	α	τ	Q_l	$ Q_c $	ϕ	f_r
a	1	0	0	-0.3	-0.3	-0.1	0.1
α	0	1	1	0	0	-0	0
τ	0	1	1	0	0	-0	0
Q_l	-0.3	0	0	1	0.8	0	-0
$ Q_c $	-0.3	0	0	0.8	1	0	0
ϕ	-0.1	0	0	0	0	1	-0.7
f_r	0.1	0	0	-0	0	-0.7	1